Finite-difference time-domain solution of second-order photoacoustic wave equation

AMIN RAHIMZADEH*, SUNG-LIANG CHEN

University of Michigan-Shanghai Jiao Tong University Joint Institute,
Shanghai Jiao Tong University, Shanghai 200240, China

*Corresponding author: amin.rahimzadeh@sjtu.edu.cn

A finite-difference time-domain numerical solution is presented for solving a single second-order photoacoustic equation, instead of solving three coupled first-order equations. In this way, we are able to insert the heating function to the simulation directly instead of initial pressure. Results are validated using k-Wave simulation and show a good agreement for future development. The perfectly matched layer boundary condition has been implemented for a second-order photoacoustic equation and results are compared to Dirichlet, Neumann and Mur boundary conditions.

Keywords: photoacoustic tomography, numerical simulation, finite-difference time-domain, second-order photoacoustic equation.

1. Introduction

Photoacoustic tomography (PAT) is a noninvasive medical imaging modality and has been widely investigated for biomedical applications [1, 2]. Photoacoustic waves are generated from an illuminated object through thermoelastic expansion. The optical absorption of different materials varies, which forms the primary contrast in photoacoustic imaging.

Reconstruction of an image is based on the detected photoacoustic waves, which are affected by some parameters related to acoustic and thermal properties of tissue, spatial distribution and time profile of a heat source. Accurate modeling of photoacoustic signals in PAT can provide a useful tool for understanding the relation between the generated photoacoustic waves and the characteristics of tissues and a heat source, and thus further optimization of PAT imaging is possible. One powerful approach is using numerical simulation to visualize propagation of photoacoustic waves.

Although a number of numerical simulation studies based on a finite element method have been investigated for modeling a photoacoustic equation so far [3–5], the finite-difference method is usually used for simulation of partial differential equations due to its convenience in implementing the code [6]. Finite-difference time-domain (FDTD) method has been studied for modeling first-order coupled acoustic wave equations in

one, two and three dimensions [7–9]. In all these works, three main first-order equations which are equation of continuity, equation of momentum conservation and pressure-density relation are solved numerically. Also, a MATLAB toolbox for simulation of photoacoustic wave fields has been developed by solving these three coupled equations, in which spatial discretization in space is based on the pseudo-spectral method and time discretization is based on central difference [7]. There are many discretization schemes in finite-difference and one of the simplest and the most common methods is central difference, which is based on expansion of Taylor series. Moreover, it has been shown that some other first-order coupled equations such as heat conduction and thermodynamic relations in fluid mechanics were added to solve a single second-order equation for more general cases [8, 9].

In this study, we performed a second-order FDTD for simulation of a single second-order photoacoustic equation. We adopted an easy central difference scheme. Compared with a more complicated and advanced scheme of pseudo-spectral discretization for solving first-order coupled photoacoustic wave equations, our method using even an easy implementing scheme of central difference for solving a second-order photoacoustic wave equation can produce acceptable results. Moreover, solving this general equation helps us directly import the heating function instead of initial pressure distribution for more complicated simulations. Besides implementing the central difference scheme for both time and space discretization, a fourth-order damping factor in space is applied for reducing oscillations. The code is validated by k-Wave MATLAB toolbox by simulation of some simple problems. The two methods show excellent agreement.

2. Modeling

2.1. Mathematical formulation

In irrotational and lossless medium, equation of motion, equation of continuity and equation of state can be written as:

$$\frac{\partial u}{\partial t} = -\frac{1}{\rho_0}\nabla P$$

$$\frac{\partial \rho}{\partial t} = -\rho_0 \nabla \cdot u \tag{1}$$

$$P = c^2\rho$$

where u is the acoustic particle velocity, ρ_0 is the ambient density, ρ is the acoustic density, c is the sound speed and P is the acoustic pressure. By combining these three coupled equations, one can get a second-order acoustic equation as

$$\left(\nabla^2 - \frac{1}{c^2}\frac{\partial^2}{\partial t^2}\right)P = 0 \tag{2}$$

Adding the time-varying heat source H to the right-hand side, Eq. (2) will result in a general photoacoustic equation in an inviscid medium

$$\left(\nabla^2 - \frac{1}{c^2}\frac{\partial^2}{\partial t^2}\right)P = -\frac{\beta}{C_p}\frac{\partial H}{\partial t} \tag{3}$$

where β denotes the volumetric coefficient of thermal expansion and C_p is specific heat capacity at constant pressure. Now, by replacing $P = -\rho\,\partial\phi/\partial t$ [10], where ϕ denotes velocity potential, an equation that can be more conveniently solved will be obtained

$$\left(\nabla^2 - \frac{1}{c^2}\frac{\partial^2}{\partial t^2}\right)\phi = \frac{\beta}{\rho C_p}H \tag{4}$$

Equation (4) is a simple second-order photoacoustic wave equation which has a source term H. For FDTD simulation, we discretize Eq. (4) using a central difference scheme in both time and space.

2.2. Discretization

For solving Eq. (4) and finding ϕ in time and two-dimensional (2-D) space, the second-order central difference discretization is used as below due to its easy implementation:

$$\frac{\partial^2\phi}{\partial x^2} = \frac{\phi_{i+1,j}^n - 2\phi_{i,j}^n + \phi_{i-1,j}^n}{\Delta x^2} + O(\Delta x^2)$$

$$\frac{\partial^2\phi}{\partial y^2} = \frac{\phi_{i,j+1}^n - 2\phi_{i,j}^n + \phi_{i,j-1}^n}{\Delta y^2} + O(\Delta y^2) \tag{5}$$

$$\frac{\partial^2\phi}{\partial t^2} = \frac{\phi_{i,j}^{n+1} - 2\phi_{i,j}^n + \phi_{i,j}^{n-1}}{\Delta t^2} + O(\Delta t^2)$$

Using the above equations, from Eq. (4) the following discretization will be obtained:

$$\frac{\phi_{i+1,j}^n - 2\phi_{i,j}^n + \phi_{i-1,j}^n}{\Delta x^2} + \frac{\phi_{i,j+1}^n - 2\phi_{i,j}^n + \phi_{i,j-1}^n}{\Delta y^2} - \frac{\phi_{i,j}^{n+1} - 2\phi_{i,j}^n + \phi_{i,j}^{n-1}}{c^2\Delta t^2} =$$

$$= \frac{\beta}{\rho C_p}H_{i,j}^n \tag{6}$$

where i, j and n are grid points in x, y and time direction, respectively. Finally, velocity potential at next level can be calculated explicitly using the following equation provided that the step sizes in x and y direction are the same ($\Delta x = \Delta y$):

$$\phi_{i,j}^{n+1} = (2 - 4\text{CFL}^2)\phi_{i,j}^n + \text{CFL}^2(\phi_{i+1,j}^n + \phi_{i-1,j}^n + \phi_{i,j+1}^n + \phi_{i,j-1}^n) +$$

$$- \phi_{i,j}^{n-1} - \frac{\beta c^2 \Delta t^2}{\rho C_p} H_{i,j}^n \tag{7}$$

where CFL $= c\Delta t/\Delta x$ is the Courant–Friedrichs–Lewy number [11]. Having the velocity potential distribution in time and space, we can calculate pressure distribution using a second-order discretization in time-domain as

$$P_{i,j}^n = -\rho \frac{\phi_{i,j}^{n+1} - \phi_{i,j}^{n-1}}{2\Delta t} + O(\Delta t^2) \tag{8}$$

According to Eqs. (5) and (8), the truncation errors are of order of two. Since second-order schemes (even-orders) are known as dispersive errors and associated with oscillation due to their dispersive characteristic, a fourth-order damping term is added to the right-hand side of Eq. (7) to reduce the oscillations

$$D = -e(\phi_{i+2,j}^n - 4\phi_{i+1,j}^n + 6\phi_{i,j}^n - 4\phi_{i-1,j}^n + \phi_{i-2,j}^n + \phi_{i,j+2}^n - 4\phi_{i,j+1}^n +$$

$$+ 6\phi_{i,j}^n - 4\phi_{i,j-1}^n + \phi_{i,j-2}^n) \tag{9}$$

where e denotes the damping coefficient and is chosen as 0.0085 in our simulation in order to get the most stable and accurate results based on the stability analysis.

2.3. Stability analysis

The value of CFL number is essential in ensuring accurate and stable results. In fact, the convergence of the solution totally relies on the value of CFL. To show the de-
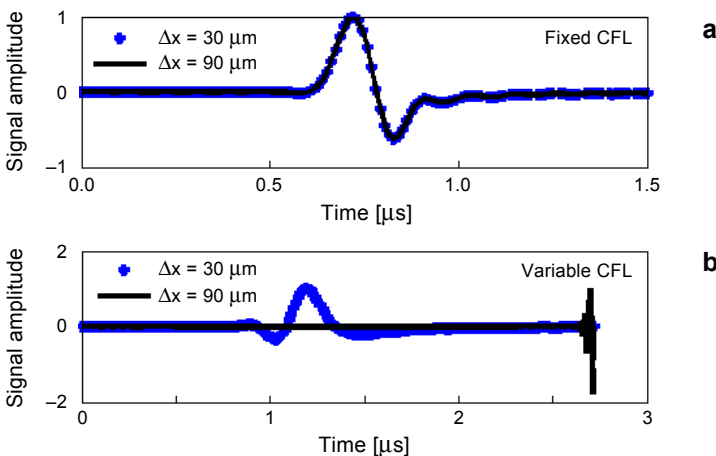

Fig. 1. Solution for a 200-μm object with two mesh sizes and fixed CFL = 0.3 – **a**, and with two mesh size and variable CFL of 0.538 (black line) and 0.194 (dotted line) – **b**.

pendence of the solution on CFL number, Fig. 1 is presented. A photoacoustic signal by illuminating a 200-μm circular absorber detected by a point detector is simulated. Figure 1**a** shows the simulated results with a fixed CFL number of 0.3 and two different mesh sizes of 30 and 90 μm. The results show that the simulated photoacoustic signal is independent of the mesh size. Therefore, we then fix the mesh size and check the results with two different CFL numbers of 0.583 and 0.194 – see Fig. 1**b**. The case with a CFL of 0.583 shows an inaccurate and unstable result (black line in Fig. 1**b**) while the case with a CFL of 0.194 shows an inaccurate result (dotted line in Fig. 1**b**). The von Neumann stability analysis indicates that to achieve stable solutions requires CFL ≤ 1 [6]. On the other hand, to get the best solution, a tradeoff between the damping coefficient and the CFL value has to be considered. A too low CFL (dotted line in Fig. 1**b**) value results in a low damping coefficient e, which cannot provide sufficient damping to the oscillations. By similar evaluation performed in the k-Wave toolbox [7], the CFL value is determined as about 0.3.

3. Results and discussion

3.1. Validation

The k-Wave uses FDTD method to solve three coupled first-order equations where Fourier collocation is applied in k-Wave discretization in spatial domain and second-order central difference scheme in time-domain. To avoid the oscillations, k-Wave applies a smooth function based on Blackman windowing to the initial pressure distribution. In this study, we try to solve a single second-order photoacoustic equation. We adopted the central difference method in both time and space domain, as described in Section 2. Similar to the k-Wave method, the Blackman windows were also applied to the second-order photoacoustic equation to circumvent the issue of oscillation besides the use of the damping factor. To validate our code, some simple examples were studied and compared.

Figure 2**a** shows a circular object located at the center within a rectangular domain which has a grid size of $\Delta x = \Delta y = 50$ μm. An infinitely short laser pulse (*i.e.*, a delta function) was used to illuminate the object. A point detector is positioned at 1 mm from the center, as shown in Fig. 2**a**. The simulated time-domain signals for 200- and 500-μm objects are shown in Figs. 2**b** and 2**c**, respectively, which present an excellent agreement between the k-Wave and second-order FDTD methods.

3.2. Example: irregular objects

To further demonstrate the generality of the developed second-order FDTD code, we also simulated two patterns of irregular objects and compared the results with those obtained by the k-Wave method.

Figure 3**a** shows a donut-shaped object with an outer diameter of 500 μm and an inner diameter of 200 μm. By placing a point detector at 1 mm from the origin, the simulated time-domain signal and its spectrum are shown in Figs. 3**b** and 3**c**, respectively. As can be seen, the two time-domain signals show good agreement. The spectra obtained
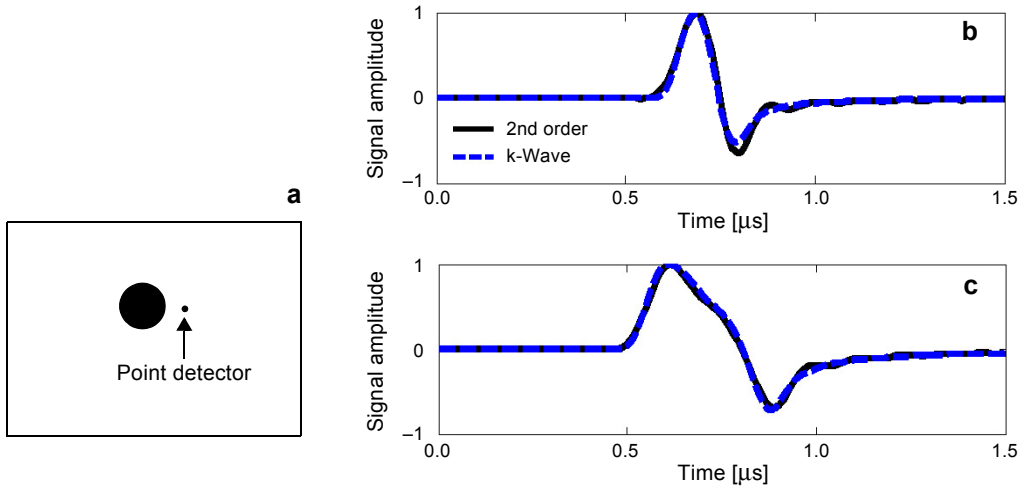
Fig. 2. Circular object within a rectangular domain and a point detector at the right side (**a**). Time-domain signal of 200-μm (**b**) and 500-μm (**c**) objects.
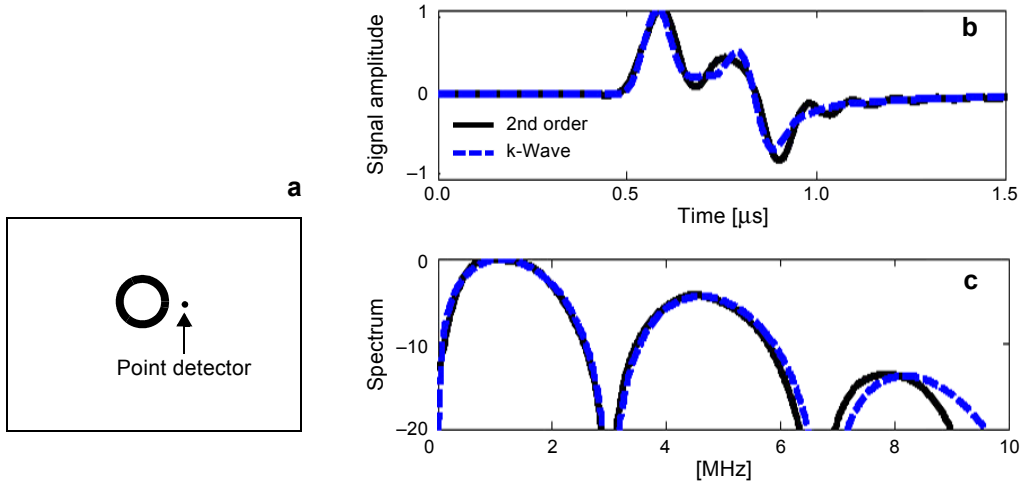

Fig. 3. Donut-shaped object and a point detector (**a**). Time-domain signal of a point detector at 1 mm from origin (**b**) and its spectrum (**c**).

by the k-Wave and second-order FDTD methods show the same central frequency of ~1 MHz in the first band.

Furthermore, another example is three 200-, 300- and 400-μm circular objects located in the rectangular domain, as shown in Fig. 4**a**. The point detector is located at 1 mm from the domain's center. The simulated time-domain signal has two peaks (Fig. 4**b**). The peak which appears earlier is from the object close to the point detector,
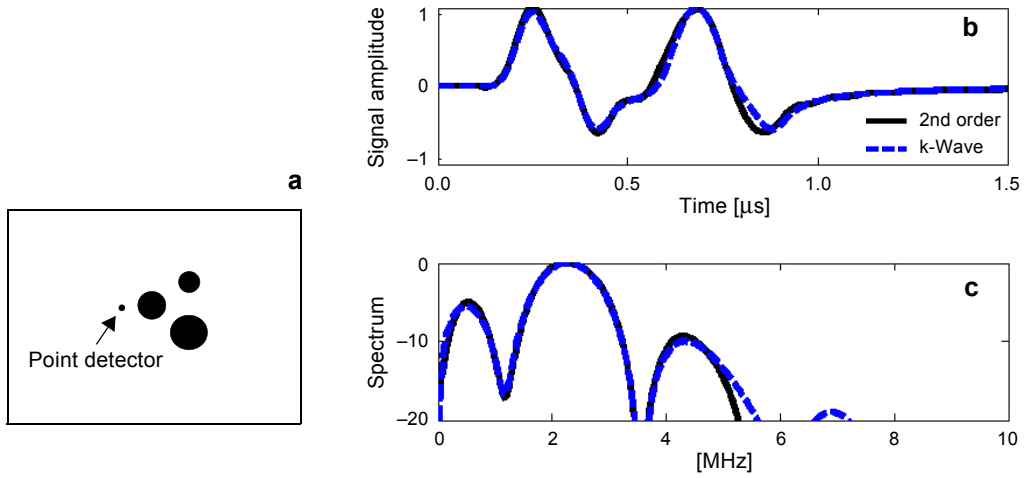
Fig. 4. Three 200-, 300- and 500-μm circular objects illuminated in a rectangular domain and a point detector (**a**). Time-domain signal (**b**) and its spectrum (**c**).
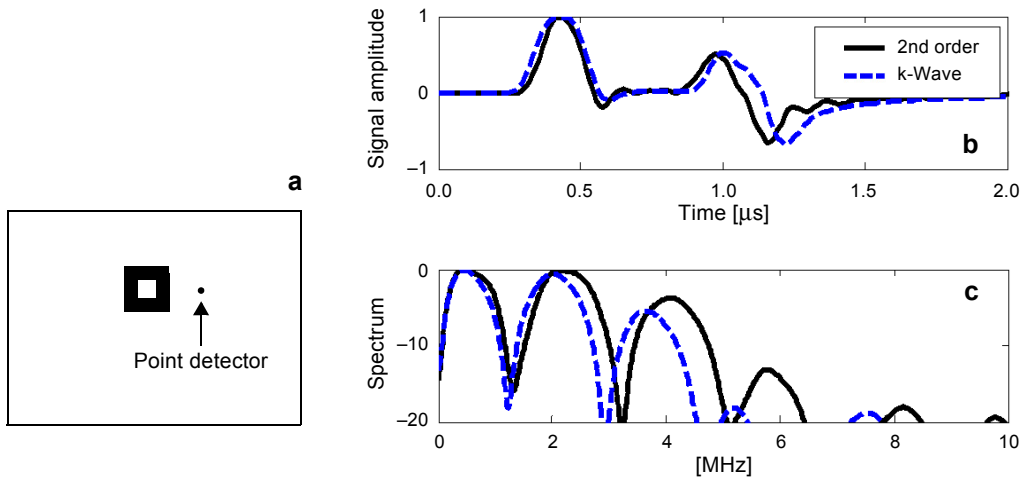

Fig. 5. Squared donut-shaped object and a point detector (**a**). Time-domain signal of a point detector at 1 mm from the origin (**b**) and its spectrum (**c**).

while the peak which appears later is a constructive summation of the waves generated by the other two objects due to their equal distances from the point detector. Also, the spectrum is shown in Fig. 4**c**.

Figure 5**a** shows a squared donut-shaped object with an outer side of 1 mm and an inner side of 400 μm to examine the scheme for another irregular shape. By placing a point detector at 1 mm from the origin, the simulated time-domain signal and its spectrum are shown in Figs. 5**b** and 5**c**, respectively. Results show that for irregular shapes,

our simulation is in a good agreement with k-Wave. For more irregular shapes such as any human organs, a mesh generation is needed before solving the domain [12]. Since the simulated signals by our scheme are in a good agreement with that by the k-Wave, the reconstructed image should be in good agreement as well.

3.3. Boundary condition

The easiest and also worst boundary condition is Dirichlet in which the pressure is equal to zero at the boundary. Neumann, Mur and perfectly matched layer (PML) are the most useful boundary conditions which are applied to wave equations modeling [7–9]. PML has been used for first-order photoacoustic coupled equations [7, 9] and reformulated for the second-order seismic wave equation [13]. In this paper PML boundary condition is applied for the second-order photoacoustic wave equation and discretized for the finite-difference method. By dividing the gradient operator into normal n and parallel to the boundary as

$$\nabla \;=\; \hat{n}\partial + \nabla^{\|} \tag{10}$$

Equation (3) in the frequency domain can be written as

$$-\frac{1}{c^2}\omega^2 P - \frac{\beta}{C_p} i\omega H \;=\; (\hat{n}\partial_n + \nabla^{\|})^2 P \tag{11}$$

By introducing a damping factor d across the PML region [13], a new complex coordinate can be defined

$$\tilde{n}(n) \;=\; n - \frac{i}{\omega}\int_0^n d(s)\,\mathrm{d}s \tag{12}$$

where,

$$\frac{\partial n}{\partial\tilde{n}} \;=\; \frac{i\omega}{i\omega + d(n)} \tag{13}$$

Generalization of Eq. (10) in a new complex coordinate results in

$$-\frac{1}{c^2}\omega^2 P - \frac{\beta}{C_p} i\omega H \;=\; (\partial_{\tilde{n}}^2 + 2\nabla^{\|}\cdot\hat{n}\partial_{\tilde{n}} + \nabla^{\|2})P \tag{14}$$

Now, by rewriting Eq. (14) in term of n

$$-\frac{1}{c^2}\omega^2 P - \frac{\beta}{C_p} i\omega H \;=\; \left[\left(\frac{\partial n}{\partial\tilde{n}}\right)^2\partial_n^2 + \frac{\partial n}{\partial\tilde{n}}2\nabla^{\|}\hat{n}\partial_n + \nabla^{\|2}\right]P \tag{15}$$

By substitution of Eq. (13), Eq. (15) is divided into three parts:

$$-\frac{1}{c^2}\omega^2 P^{(1)} - \frac{\beta}{C_p}i\omega H^{(1)} = \frac{-\omega^2}{(i\omega+d)^2}\partial_n^2 P$$

$$-\frac{1}{c^2}\omega^2 P^{(2)} - \frac{\beta}{C_p}i\omega H^{(2)} = \frac{2i\omega}{i\omega+d}\nabla^{\|}\hat{n}\partial_n P \qquad (16)$$

$$-\frac{1}{c^2}\omega^2 P^{(3)} - \frac{\beta}{C_p}i\omega H^{(3)} = \nabla^{\|2} P$$

where, $P = P^{(1)} + P^{(2)} + P^{(3)}$ and $H = H^{(1)} + H^{(2)} + H^{(3)}$. Now, converting back to the time-domain, we get:

$$\frac{1}{c^2}(\partial_t + d)^2 P^{(1)} - \mathrm{sgn}(t)(\partial_t + d)^2 H^{(1)} = \partial_n^2 P$$

$$\frac{1}{c^2}\partial_t(\partial_t + d)P^{(2)} - \frac{\beta}{C_p}(\partial_t + d)H^{(2)} = \nabla^{\|}\hat{n}\partial_n P \qquad (17)$$

$$\frac{1}{c^2}\partial_t^2 P^{(3)} - \frac{\beta}{C_p}\partial_t H^{(3)} = \nabla^{\|2} P$$

Since damping profile sets to be zero at computation domain, Eq. (17) will be the same as Eq. (3); however at PML region one needs to solve Eq. (17) in order to damp the waves at boundaries. The effectiveness of PML relies on the number of layers N and the damping profile. Here we use the damping profile of

$$d(n) = \frac{3c}{N\Delta x}\left(\frac{x}{\delta}\right)^2 \qquad (18)$$

in x direction and

$$d(n) = \frac{3c}{N\Delta y}\left(\frac{y}{\delta}\right)^2 \qquad (19)$$

in y direction, where δ is the PML thickness.

Figure 6 shows the effect of PML boundary condition and how it absorbs photoacoustic waves of a delta pulse illumination of a circular object in the middle of 6×6 mm domain (Fig. 6**a**). The two upper and lower boundaries are PML with 10 layers while we used the Dirichlet boundary condition at left and right boundaries. Photoacoustic waves propagate toward the boundaries uniformly after 1.7 µs as is shown in Fig. 6**b**.
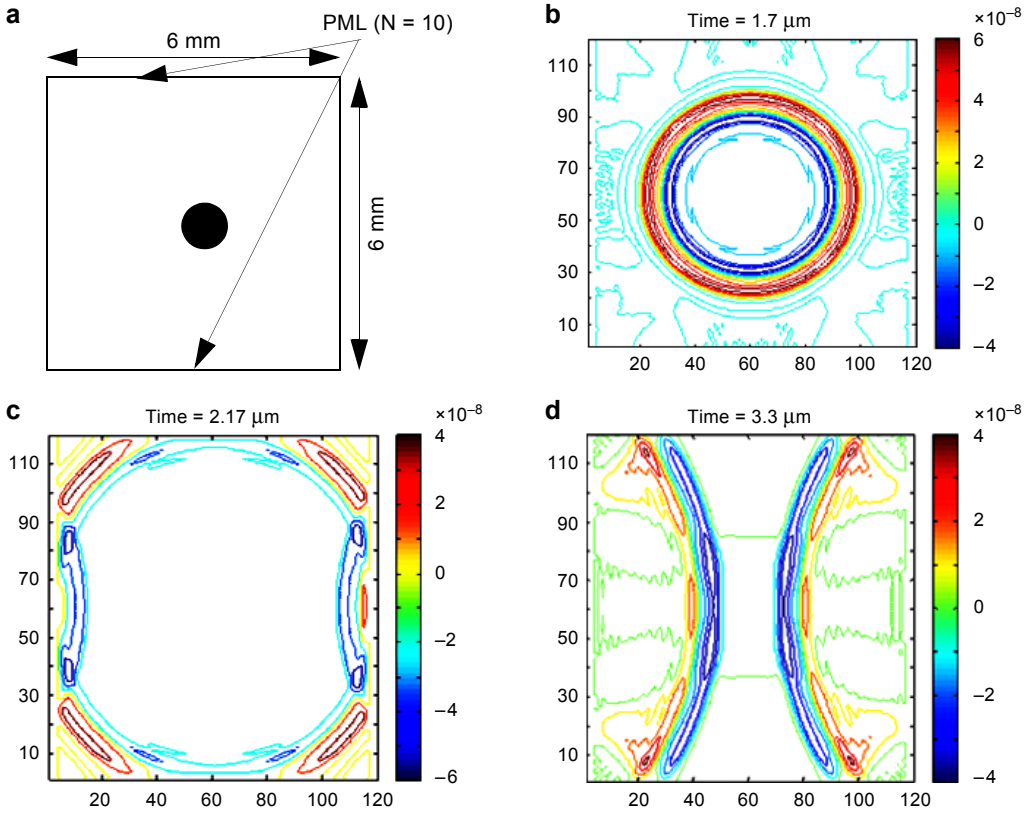
Fig. 6. Effect of PML boundary condition for a circular object in 6 × 6 mm domain in which the upper and lower boundary condition is PML with 10 layers and the other is Dirichlet boundary condition (**a**). Propagating photoacoustic waves after 1.7 µs (**b**), 2.17 µs (**c**) and 3.3 µs (**d**).
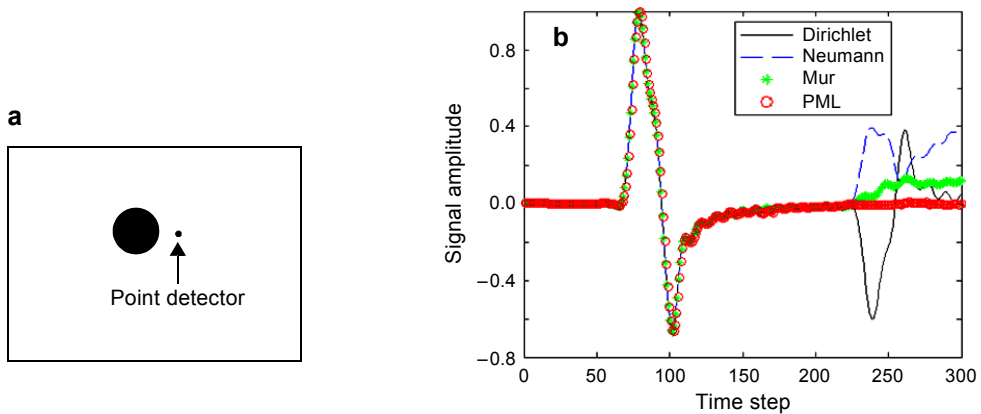

Fig. 7. Comparison of the effect of different boundary conditions on photoacoustic signal. Circular object within a rectangular domain and a point detector at the right side (**a**), and photoacoustic signals detected by a point detector (**b**).

After 2.17 μs the waves reach to the boundaries and start to be absorbed by PML region and reflected by the other boundaries (Fig. 6**c**). Figure 6**d** shows that after 3.3 μs the reflected waves from the left and right boundaries are back to the domain while they have been absorbed by the PML regions.

PML boundary condition has a significant advantage over other boundary conditions and this advantage is shown in Fig. 7. A circular object in the rectangular domain is illuminated by a delta pulse excitation and a point detector records the photoacoustic signal (Fig. 7**a**). When the propagating wave reaches the boundaries, PML boundary region will absorb it while other boundaries reflect it back to the domain. The Mur boundary condition has an acceptable result considering its simplicity (Fig. 7**b**).

4. Conclusions

The simulation of photoacoustic phenomena is a very important and useful tool for investigation of photoacoustic signals affected by different factors such as tissue properties. Thus, the simulation is also helpful to study PAT image reconstruction. We presented an easy central difference FDTD method to solve the single second-order photoacoustic equation instead of three coupled first-order equations. To validate our code, solutions of two simple problems were compared with k-Wave toolbox. Also, two relatively complicated examples have been investigated and good agreement between the second-order FDTD and k-Wave methods is observed. Boundary condition is one important issue that helps reducing computation time by decreasing computational domain. Absorbing boundary conditions such as PML will make this desire come true.

In the present work we implemented PML absorbing boundary condition for the second-order photoacoustic equation and discretized it for FDTD solution. Furthermore, results have been compared with Dirichlet, Neumann and Mur boundary conditions. Future work may focus on developing our code for a more complicated case such as photoacoustic wave propagation in media with inhomogeneous acoustic properties.

References

[1] LIHONG V. WANG, *Multiscale photoacoustic microscopy and computed tomography*, Nature Photonics **3**(9), 2009, pp. 503–509.

[2] LIANGZHONG XIANG, BO WANG, LIJUN JI, HUABEI JIANG, *4-D photoacoustic tomography*, Scientific Reports **3**, 2013, article 1113.

[3] ZHEN YUAN, HONGZHI ZHAO, CHANGFENG WU, QIZHI ZHANG, HUABEI JIANG, *Finite-element-based photoacoustic tomography: phantom and chicken bone experiments*, Applied Optics **45**(13), 2006, pp. 3177–3183.

[4] BAUMANN B., WOLFF M., KOST B., GRONINGA H., *Finite element calculation of photoacoustic signals*, Applied Optics **46**(7), 2007, pp. 1120–1125.

[5] LEI YAO, HUABEI JIANG, *Finite-element-based photoacoustic tomography in time domain*, Journal of Optics A: Pure and Applied Optics **11**(8), 2009, article 085301.

[6] HOFFMANN K.A., CHIANG S.T., *Computational Fluid Dynamics*, 4th Ed., Vol. 2, Engineering Education System, 2000.

[7] Treeby B.E., Cox B.T., *k-Wave: MATLAB toolbox for the simulation and reconstruction of photoacoustic wave field*, Journal of Biomedical Optics **15**(2), 2010, article 021314.

[8] Deng-Huei Huang, Chao-Kang Liao, Chen-Wei Wei, Pai-Chi Li , *Simulations of optoacoustic wave propagation in light-absorbing media using a finite-difference time-domain method*, The Journal of the Acoustical Society of America **117**(5), 2005, pp. 2795–2801.

[9] Yae-Lin Sheu, Pai-Chi Li, *Simulations of photoacoustic wave propagation using a finite-difference time-domain method with Berenger's perfectly matched layers*, The Journal of the Acoustical Society of America **124**(6), 2008, pp. 3471–3480.

[10] Wang L.V., Wu H.-I., *Photoacoustic tomography*, [In] *Biomedical Optics*, Wiley, 2009, pp. 283–321.

[11] Courant R., Friedrichs K., Lewy H., *Über die partiellen Differenzengleichungen der mathematischen Physik*, Mathematische Annalen **100**(1), 1928, pp. 32–74.

[12] Sanmiguel-Rojas E., Ortega-Casanova J., del Pino C., Fernandez-Feria R., *A Cartesian grid finite-difference method for 2D incompressible viscous flows in irregular geometries*, Journal of Computational Physics **204**(1), 2005, pp. 302–318.

[13] Komatitsch D., Tromp J., *A perfectly matched layer absorbing boundary condition for the second -order seismic wave equation*, Geophysical Journal International **154**(1), 2003, pp. 146–153.